coatings

MDPI

Article

Investigations of Microstructures and Erosion–Corrosion Performance of Cast Boron-Bearing Stainless Steel

Dawei Yi [1,*], Bin Li [1,*], Xiao Tan [2], Sifan Liu [1], Jin Chen [1] and Yefei Li [3,*]

[1] College of Materials Science and Engineering, Xi'an University of Science and Technology, Xi'an 710054, China; Sifan433320@163.com (S.L.); chenjin85056@163.com (J.C.)
[2] Department of Railway Locomotive, Heilongjiang Communitications Polytechnic, Qiqihaer 161000, China; ldtanxiao86@163.com
[3] State Key Laboratory for Mechanical Behavior of Materials, College of Materials Science and Engineering, Xi'an Jiaotong University, Xi'an 710049, China
* Correspondence: yidawei19820608@163.com (D.Y.); lb18709267708@163.com (B.L.); liyefei@xjtu.edu.cn (Y.L.); Tel.: +86-29-85587373 (D.Y.)

Abstract: The microstructures and erosion–corrosion properties of boron-bearing stainless steel were researched by an erosion–corrosion tester, energy dispersive X–ray spectrometry, scanning electron microscope and X-ray diffraction analysis. The microstructures of as-cast, boron-bearing stainless steel contain $M_7(B,C)_3$, $M_2(B,C)$ borocarbides and the martensite matrix; the matrix has less chromium and more nickel than those in the $M_2(B,C)$ and $M_7(B,C)_3$. The microstructures in heat-treated, boron-bearing stainless steel consist of $M_7(B,C)_3$, $M_2(B,C)$ and $M_{23}(B,C)_6$ borocarbides and ferrite, and the Rockwell hardness of heat-treated, boron-bearing stainless steel is lower than that of as-cast steel. For Cr28 white cast iron and boron-bearing stainless steel, the mixing wheel with higher rotating speed leads to a higher erosion–corrosion weight loss, and as the impingement angle increases, the erosion–corrosion weight loss increases first, and then decreases. For any erosion–corrosion experiment conditions, the erosion–corrosion resistance of boron-bearing stainless steel is better than that of Cr28 white cast iron.

Keywords: boron-bearing stainless steel; microstructure; hardness; erosion–corrosion

Citation: Yi, D.; Li, B.; Tan, X.; Liu, S.; Chen, J.; Li, Y. Investigations of Microstructures and Erosion–Corrosion Performance of Cast Boron-Bearing Stainless Steel. *Coatings* **2021**, *11*, 1553. https://doi.org/10.3390/coatings11121553

Academic Editor: Alina Vladescu

Received: 18 November 2021
Accepted: 14 December 2021
Published: 17 December 2021

1. Introduction

Slurry pump impellers, turbine runners, pipelines, etc., have been eroded and corroded by corrosive media for a long time [1–6]. The strong interaction between erosion and corrosion leads to serious damage to the materials and reduces the life of the materials [7–10]. The eutectic carbides with a high hardness in high chromium cast irons gives these irons an excellent wear resistance [11–16]. The corrosion resistance of high-chromium cast iron is enhanced by the chromium element, so that these cast irons can be used in corrosive wear conditions [17]. Zhang et al. [18,19] studied the mechanism and electrochemical behavior of the inter-phase corrosion of chromium white cast irons. The results showed that the inter-phase corrosion between the carbide and matrix in chromium white cast iron caused serious injury to the matrix and made the carbides exposed in strong acidic media conditions. Without matrix support, the carbides must be broken by flow slurry, which drastically reduced the erosion and corrosion resistance for the chromium white cast iron. The development of new erosion- and corrosion-resistant materials will help reduce the loss of flow-passing parts.

Many research works on Fe-B cast alloys were carried out because of its excellent wear properties [20–25]. Fu et al. [22] studied the microstructures and mechanical properties of austenitic stainless steel containing the B element under different austenitizing temperatures. The results showed that there were borocarbide ($M_2(B,C)$) and austenite in heat-treated, boron-bearing stainless steel. The increase in the austenization temperature

increased the Vickers hardness of boron-bearing stainless steel and did not clearly affect the impact toughness. Jian et al. [26] studied the two-body abrasive wear performance of Fe-3.0 wt.% B cast alloy, which contained the chromium element. It could be seen from the results that the fracture toughness of M_2B and wear performance of Fe-B cast alloy could be improved by chromium element. Zhang et al. [27] investigated the microstructures and abrasion wear performance of the Fe-B alloy under a hot forging process. It could be seen from the results that the hardness and toughness of the unforged samples were both lower than those of the forged samples. For hard abrasive wear test conditions, the wear performance of unforged Fe-B alloy was not significantly different from that of forged alloy.

The chromium and nickel elements in stainless steel could form an oxide film, which could improve corrosion resistance [28]. Moreover, for the H_2SO_4 acid solution, the corrosion resistance of the stainless steel could be improved by the boriding treatment [29,30]. Based on the above research results, the microstructures and erosion–corrosion property of boron-bearing stainless steel were studied, and the erosion–corrosion mechanism was also researched.

2. Experiments and Tests

2.1. Test Alloy Preparation

Boron-bearing stainless steel was smelted in a 10 kg induction furnace (Luoyang Braveman Special Testing Furnace Co. Ltd., Luoyang, China). All the raw materials, consisting of Fe-55.2 wt.% Cr alloy, Fe-74.3 wt.% Si alloy, Fe-59.3 wt.% Mn alloy, nickel board, pure iron and steel block, were smelted in the furnace. When the temperature in molten steel was 1650 °C, the Fe-15.6 wt.% B alloy was added to the furnace. After deoxidizing with pure aluminum, the molten steel was transferred to the ladle. When the temperature was reduced to 1480 °C, the molten steel was transferred to a sand mold. In the heat treatment process, all the samples were heated to 850 °C for 2 h in an inbox-type resistance furnace, and then cooled in air. Based on the analysis of inductively coupled plasma optical emission spectroscopy (Agilent Technologies Inc., Santa Clara, CA, USA), the chemical compositions of the boron-bearing stainless steel are shown in Table 1.

Table 1. Chemical components of boron-bearing stainless steel (wt.%).

Element	C	B	Cr	Ni	Si	Mn	P	S	Fe
Content	0.16	1.58	17.32	0.53	0.64	0.67	0.03	0.03	Bal.

2.2. Microstructure Analysis

The geometries of the sample A and B are shown in Figure 1. A metallographic analysis was carried out on sample A (dimension 20 mm × 20 mm × 10 mm). In metallographic analysis process, the mixture containing 45 mL 4% Picral, 5 mL HCl and 50 mL 5% nital was selected to etch the polished surface on sample A. The Tescan Vegaiixmu scanning electron microscope (Tescan Ltd., Brno, Czech Republic), attached to an energy dispersive X-ray spectrometry (OXFORD 7718, Tescan Ltd., Brno, Czech Republic), was selected to analyze microstructures. The D/MAX–2400 diffractometer (Rigaku Corporation, Tokyo, Japan) attaching copper Kα radiation at 40 kV and 30 mA as X-ray source was selected to identify the phases in test steel. The samples were analyzed in a 2θ range from 10° to 90° (0.02° per step).

2.3. Hardness Measurements

The Rockwell hardness of the test steel was analyzed by HRS–150 hardness tester (Shanghai Wanheng Precision Instruments Co. Ltd., Shanghai, China), 1470 N was selected as test load). The average of 10 values was considered to be the test result. The HXD–1000TMC tester (Shanghai Wanheng Precision Instruments Co. Ltd., Shanghai, China) was chosen to analyze the microindentation hardness by complying with ASTM standard E384–08 [31]. The hardnesses of the matrix and borocarbide were tested by using 0.49 N and

0.98 N, respectively; the test force lasted for 10 s. The average of 20 values was considered to be the result.

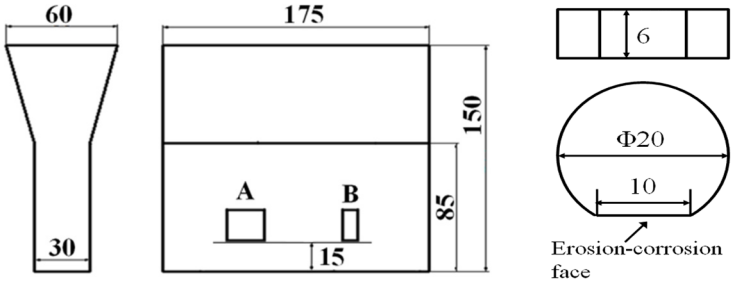

Figure 1. Geometric sizes of Y block (**a**) and erosion–corrosion sample (**b**) (in mm).

2.4. Erosion–Corrosion Tests

In the slurry, an erosion–corrosion tester (Xiangyu Machinery Processing Co. Ltd., Xi'an, China) was used to investigate the erosion–corrosion performance of boron-bearing stainless steel. In present research, the contrast material was Cr28 white cast iron (2.48C-27.82Cr-2.32Mo, wt.%, 60.8 ± 0.7 HRC). The physical design of the erosion–corrosion testing machine is shown in Figure 2. The geometric sizes of the erosion–corrosion testing sample B (as shown in Figure 1a) are shown in Figure 1b. The erosion–corrosion face on sample B was polished for the erosion–corrosion experiment. The revolving speeds (rev·min^{-1}) of mixing wheel (as shown in Figure 2) were selected at 1200 and 1700, respectively. The distance L (in Figure 2) between mixing wheel center and erosion–corrosion sample B was set to 80 mm. The mixture containing 8000 mL, 2.4% sulfuric acid solution and 3 kg quartz sand (SiO_2, 900–1100 HV [32], the size was 0.61 ± 0.13 mm) was used as the erosion–corrosion slurry, and the percentage of sulfuric acid in the slurry was 1.7%. Based on the cooling water, the temperature in the slurry was limited to 20 ± 1 °C in the test process. The impingement angles (as shown in Figure 2) containing 0°, 30°, 45° and 60° were designed for erosion–corrosion samples. The test time of erosion–corrosion experiment was 180 min. The electronic balance (the accuracy was 0.1 mg) was chosen to analyze the erosion–corrosion weight loss in the sample. The weight loss average of three samples was regarded as the experiment result.

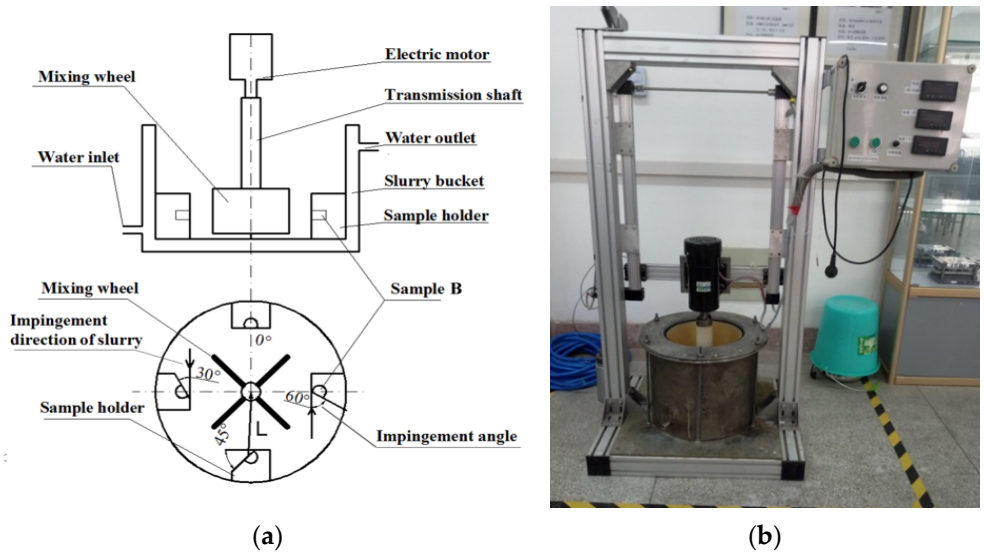

Figure 2. Structure drawing of erosion–corrosion test equipment: (**a**) structure drawing; (**b**) physical map.

3. Results and Discussions

3.1. As-Cast Microstructure

The matrix and borocarbides (Figure 3) are the main microstructures in boron-bearing stainless steel. The $M_7(B,C)_3$ and $M_2(B,C)$ (M stands for chromium and iron elements [21]) detected by XRD (Figure 4) exist in the test steel. The borocarbide morphologies of $M_2(B,C)$, $M_7(B,C)_3$ are meshed and rod-shaped (Figure 3). The microindentation hardness and rockwell hardness test results are shown in Table 2. The matrix in test steel is confirmed as martensite by a microindentation hardness test. The EDS analysis reveals that $M_2(B,C)$ borocarbide contains more chromium element than that in martensite matrix (Figure 3c), and there is more nickel element in the matrix than that in $M_2(B,C)$ borocarbide (Figure 3d). Moreover, the matrix has less chromium and more nickel than those in $M_7(B,C)_3$ borocarbide, respectively.

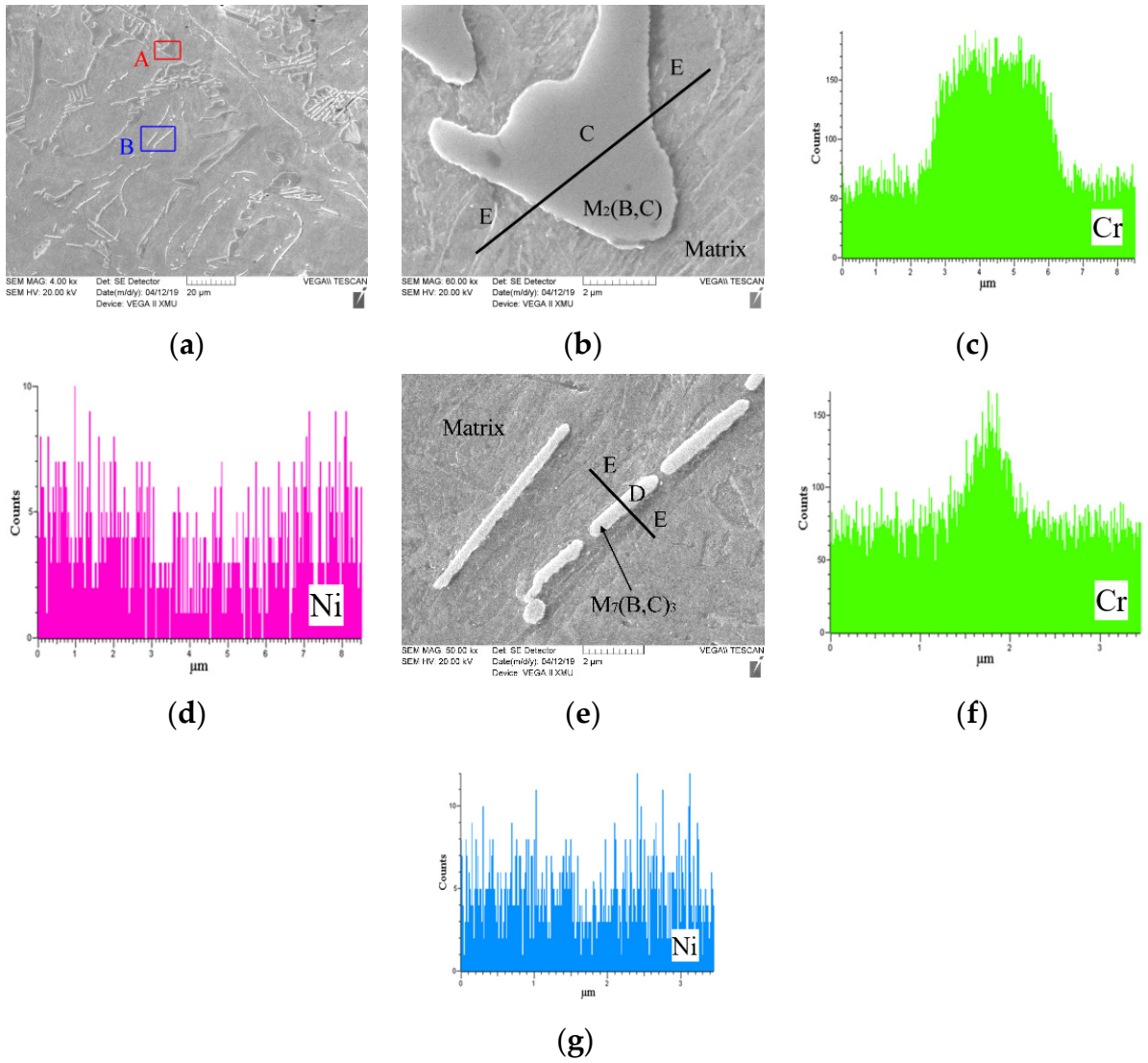

Figure 3. The as-cast microstructure and EDS analyses of boron-bearing stainless steel: (**a**) the microstructure morphology of as-cast boron-bearing stainless steel; (**b**) displaying microstructure morphology of A area: C-borocarbide [$M_2(B,C)$], E-matrix; (**c**,**d**) displaying the distributions of chromium and nickel elements along black line in (**b**), respectively; (**e**) displaying the morphology of B area: D-borocarbide [$M_7(B,C)_3$], E-matrix; (**f**,**g**) displaying the distributions of chromium and nickel elements along black line in (**e**), respectively.

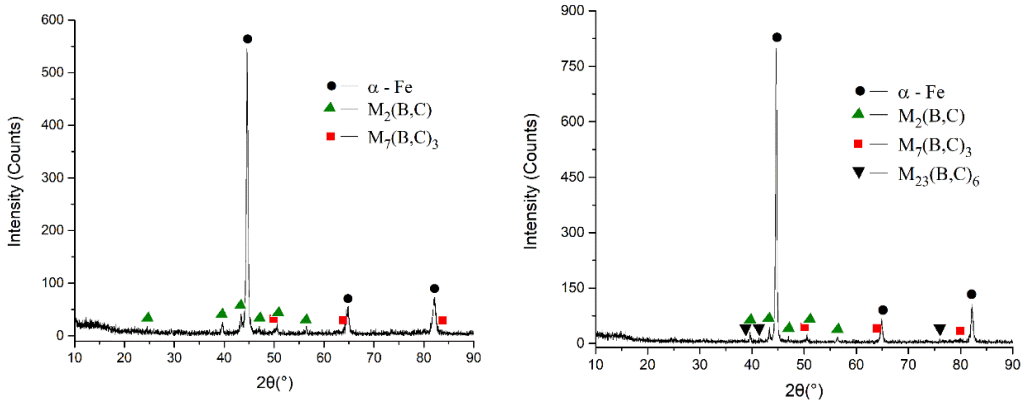

Figure 4. X-ray diffraction spectrums of as-cast (**a**) and heat-treated, (**b**) boron-bearing stainless steel.

Table 2. Hardnesses of the microstructures and boron-bearing stainless steel.

Samples	Parameters	Average	Deviation
As-cast	Matrix (HV)	534	11
	M_2(B,C) (HV)	1558	16
	Steel (HRC)	50.2	0.7
Heat-treated	Matrix (HV)	307	9
	M_2(B,C) (HV)	1563	18
	Steel (HRC)	29.6	0.6

3.2. Heat-Treated Microstructure and Hardness

Figure 5 reveals that the borocarbides and the ferrite (290–320 HV) matrix appear in the heat-treated boron-bearing stainless steel. The borocarbides are proven to be M_{23}(B,C)$_6$, M_2(B,C) and M_7(B,C)$_3$ by XRD (Figure 4b), respectively. The morphologies of M_{23}(B,C)$_6$, M_7(B,C)$_3$ and M_2(B,C) borocarbides are granular, rod-shaped and meshed, respectively. There is no clear difference between the hardness of heat-treated M_2(B,C) and the hardness of as-cast M_2(B,C). In comparison with martensite matrix in as-cast steel, the ferrite matrix decreases the Rockwell hardness of heat-treated steel (as shown in Table 2).

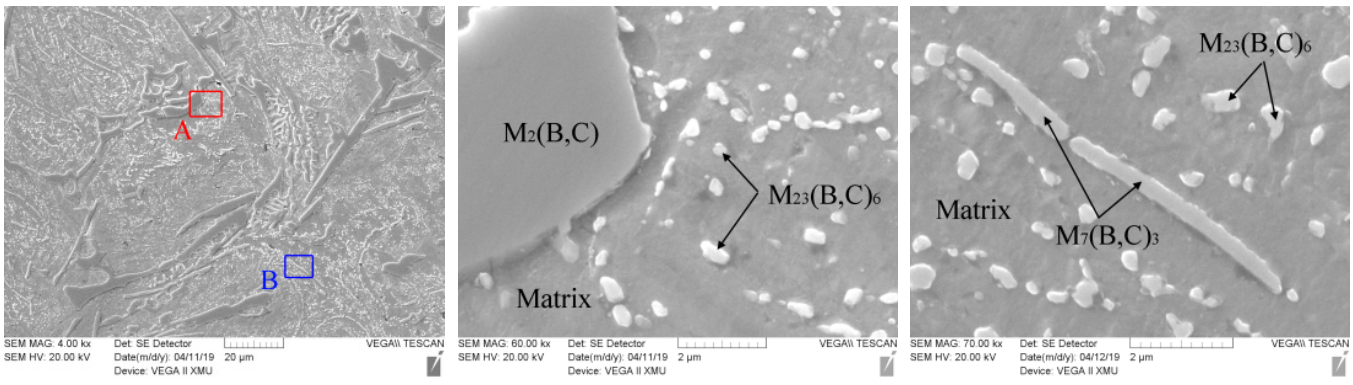

Figure 5. The microstructure analysis of heat-treated boron-bearing stainless steel: (**a**) the heat-treated microstructures; (**b**) displaying the microstructures of A area in (**a**); (**c**) displaying the microstructures of B area in (**a**).

3.3. Erosion–Corrosion Experiment Analysis

The contrast of erosion–corrosion weight losses of the boron-bearing stainless steel and Cr28 white cast iron is finished (as shown in Figure 6). The erosion–corrosion face

morphologies of test steel and Cr28 samples can be seen in Figures 7–9. The $M_2(B,C)$ borocarbide has a hardness of H_1 (1545–1585 HV), and the quartz sand abrasive (SiO_2) has a hardness of H_2 (900–1100 HV [32]). Based on the ratio ($H_1/H_2 > 1$), the quartz sand is classified as soft abrasive [33]. The SiO_2 particles cannot plough the borocarbide, while the impact of SiO_2 particles will crash the borocarbide. The ferrite matrix (H_3) has a hardness of less than 320 HV. Based on the ratio ($H_3/H_2 < 0.8$), the quartz sand is classified as hard abrasive. The SiO_2 particle with a high hardness can plough the ferrite matrix. According to the same calculation and analysis method, for the carbide (1490–1550 HV) and matrix (660–700 HV) in Cr28 white cast iron, the SiO_2 particles are regarded as soft abrasive and hard abrasive, respectively. The matrix can be ploughed by SiO_2 particles, and the impact of SiO_2 particles will crash the carbide.

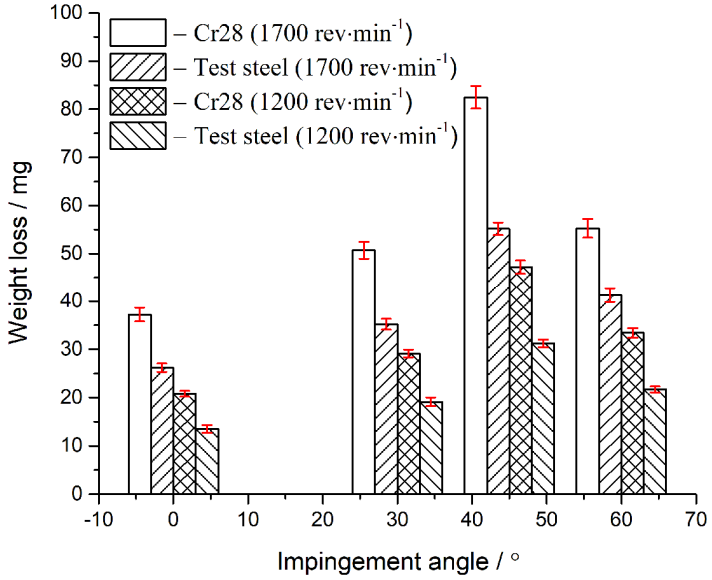

Figure 6. The erosion–corrosion weight loss analysis of the Cr28 white cast iron and boron-bearing stainless steel.

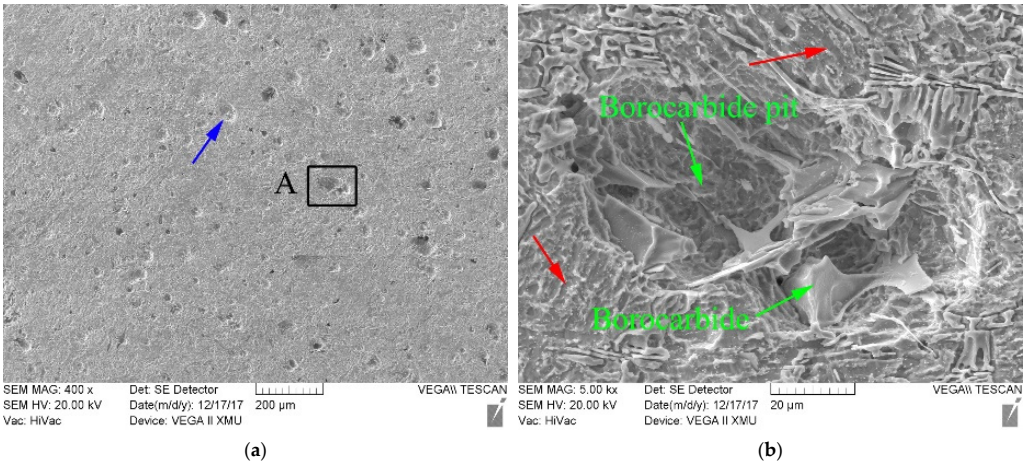

(**a**) (**b**)

Figure 7. Erosion–corrosion face morphology SEM of boron-bearing stainless steel sample under test condition of impingement angle 45°, and rotating speed 1200 rev·min^{-1}: (**a**) displaying erosion–corrosion face morphology; (**b**) displaying the magnified microstructures of A area.

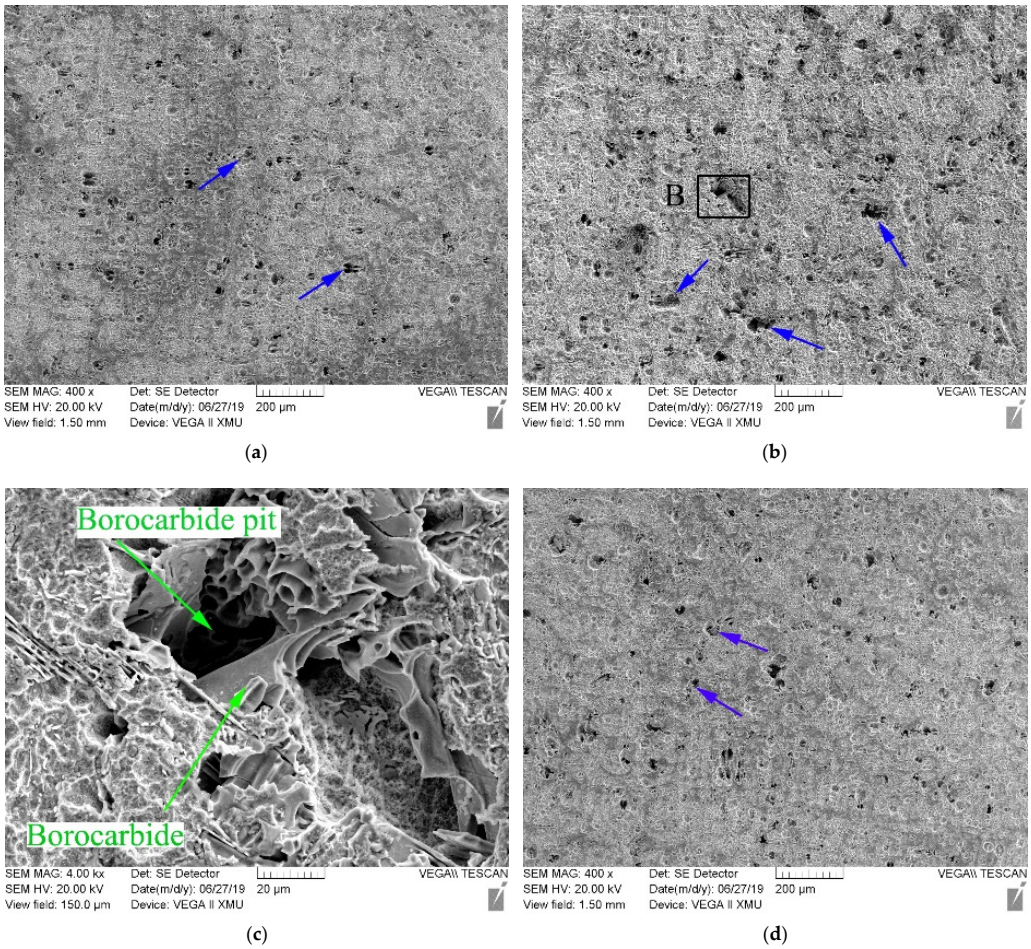

Figure 8. Erosion–corrosion face morphology SEM of boron-bearing stainless steel sample under test condition of rotating speed 1700 rev·min^{-1}: impingement angles contain 0° (**a**), 45° (**b**) and 60° (**d**); (**c**) displaying the magnified microstructures of B area.

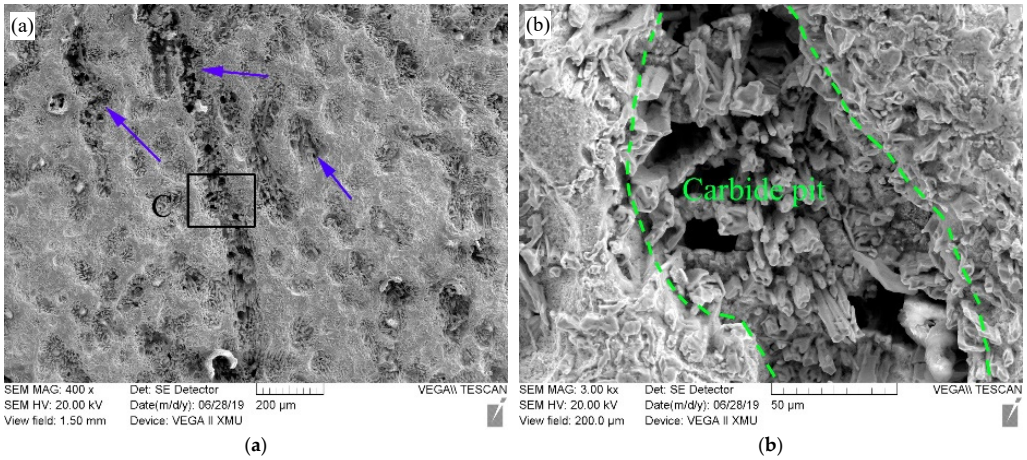

Figure 9. Erosion–corrosion face morphology SEM of Cr28 white cast iron sample under test condition of impingement angle 45°, and rotating speed 1700 rev·min^{-1}: (**a**) displaying erosion–corrosion face morphology; (**b**) displaying the magnified microstructures of C area.

When the impingement angle is set to 45° and the rotating speed is set to 1200 rev·min^{-1}, many pits (the position of the blue arrow in Figure 7a) and scraping traces (the position of the red arrow in Figure 7b) exist in the erosion–corrosion face of boron-bearing stainless steel samples. When the face of the sample is eroded and corroded by slurry, the scraping

of SiO_2 particles causes the scrape trace to appear in ferrite matrix. The erosion and corrosion damages of the matrix make the borocarbide exposed. The impact of SiO_2 particles can break the exposed borocarbide and cause pits (Figure 7b) to appear on the erosion–corrosion face.

For Cr28 white cast iron and boron-bearing stainless steel, the mixing wheel with a higher rotating speed leads to a higher erosion–corrosion weight loss (as shown in Figure 6). For boron-bearing stainless steel, compared with Figure 7a (blue arrow), the characteristics of the borocarbide pit in Figure 8b (blue arrows) are larger and more numerous. This phenomenon has a positive relationship with Figure 6. The reason for this is that the impact velocity of the slurry is increased by the mixing wheel possessing a higher rotating speed. The damages to the matrix and borocarbide can be exacerbated by the slurry with a higher impact velocity, which makes the erosion–corrosion weight loss become higher.

As the impingement angle increases, the erosion–corrosion weight loss increases first and then decreases. Under the impingement angle of 45°, the erosion–corrosion weight losses of boron-bearing stainless steel and Cr28 white cast iron are higher (Figure 6), respectively. Corresponding to the erosion–corrosion weight loss curve in Figure 6, for boron-bearing stainless steel, compared to a 0° or 60° impingement angle (blue arrows in Figure 8a,d), more fragmentized borocarbides and larger borocarbide pits appear in the erosion–corrosion face when the impingement angle is 45° (blue arrows in Figure 8b). These research results show that, when the impingement angle is 45°, the test material must be eroded and corroded more severely than at 0°, 30° and 60° impingement angles.

For any experiment conditions, the erosion–corrosion weight losses of boron-bearing stainless steel samples are less than those of Cr28 white cast iron samples (it can be seen in Figure 6). For Cr28 white cast iron samples (1700 $rev \cdot min^{-1}$ is selected as mixing wheel rotating speed, and 45° is selected as impingement angle), the slurry erodes and corrodes the matrix severely, breaks more carbides, and creates some large carbide pits, which are left in the erosion–corrosion face (blue arrows in Figure 9a). In comparison, the borocarbides in the erosion–corrosion face of boron-bearing stainless steel are broken slightly, and the borocarbide pits are smaller (blue arrows in Figure 8b). Therefore, the erosion–corrosion property of boron-bearing stainless steel are better.

4. Conclusions

(1) The as-cast boron-bearing stainless steel contains martensite, $M_7(B,C)_3$ borocarbide and $M_2(B,C)$ borocarbide. In comparison with the martensite matrix, the $M_7(B,C)_3$ and $M_2(B,C)$ borocarbides possess less nickel and more chromium.

(2) The ferrite and $M_{23}(B,C)_6$, $M_2(B,C)$, $M_7(B,C)_3$ borocarbides are the main microstructure in heat-treated, boron-bearing stainless steel. Compared with martensite matrix in as-cast steel, the ferrite matrix decreases the rockwell hardness of heat-treated test steel.

(3) Under any test conditions, the erosion–corrosion weight loss of boron-bearing stainless steel is lower than that of Cr28 white cast iron, and the boron-bearing stainless steel shows a better erosion–corrosion resistance.

Author Contributions: Conceptualization, D.Y. and B.L.; methodology, D.Y. and X.T.; formal analysis, B.L. and S.L.; investigation, D.Y., B.L. and X.T.; data curation, D.Y. and S.L.; writing—original draft preparation, D.Y. and J.C.; supervision, S.L., J.C. and Y.L. All authors have read and agreed to the published version of the manuscript.

Funding: This research was funded by the National Natural Science Foundation of China, grant number 51705414; the Natural Science Basic Research Program of Shaanxi, grant number 2020JM-516.

Institutional Review Board Statement: Not applicable.

Informed Consent Statement: Not applicable.

Data Availability Statement: Data is contained within the article.

Acknowledgments: The authors were grateful for the support provided by the College of Materials Science and Engineering, Xi'an University of Science and Technology.

Conflicts of Interest: The authors declare no conflict of interest.

References

1. Yoganandh, J.; Natarajan, S.; Kumaresh Babu, S.P. Erosive wear behavior of nickel-based high alloy white cast iron under mining conditions using orthogonal array. *J. Mater. Eng. Perform.* **2013**, *22*, 2534–2541. [CrossRef]
2. Zhang, H.; Tan, Y.Q.; Yang, D.M.; Trias, F.X.; Jiang, S.Q.; Sheng, Y.; Oliva, A. Numerical investigation of the location of maximum erosive wear damage in elbow: Effect of slurry velocity, bend orientation and angle of elbow. *Powder Technol.* **2012**, *217*, 467–476. [CrossRef]
3. Lin, Y.C.; Chang, K.Y. Elucidating the microstructure and erosive wear of ceramic powder alloying on AISI1050 steel. *Surf. Coat. Technol.* **2012**, *207*, 493–502. [CrossRef]
4. Ramesh, C.S.; Devaraj, D.S.; Keshavamurthy, R.; Sridhar, B.R. Slurry erosive wear behaviour of thermally sprayed Inconel-718 coatings by APS process. *Wear* **2011**, *271*, 1365–1371. [CrossRef]
5. Salehikahrizsangi, P.; Raeissi, K.; Karimzadeh, F.; Calabrese, L.; Proverbio, E. Effects of surface morphology on erosion–corrosion and corrosion resistance of highly hydrophobic nickel-tungsten electrodeposited film. *Coatings* **2021**, *11*, 1084. [CrossRef]
6. Kevin, P.S.; Tiwari, A.; Seman, S.; Mohamed, S.A.B.; Jayaganthan, R. Erosion-corrosion protection due to Cr_3C_2-NiCr cermet coating on stainless steel. *Coatings* **2020**, *10*, 1042. [CrossRef]
7. Xing, J.D.; Gao, Y.M.; Zhang, G.S. Investigation to erosion-corrosion behavior of stainless steel and high carbon steel. *J. Xi'an Jiaotong Univ.* **2004**, *38*, 469–473.
8. Shivamurthy, R.C.; Kamaraj, M.; Nagarajan, R.; Shariff, S.M.; Padmanabham, G. Influence of microstructure on slurry erosive wear characteristics of laser surface alloyed 13Cr–4Ni steel. *Wear* **2009**, *267*, 204–212. [CrossRef]
9. Wan, W.C.; Xiong, J.; Guo, Z.X.; Du, H.; Tang, L.M. Erosive wear behavior of Ti(C,N)-based cermets containing different Cr_3C_2 addition in slurry conditions. *Int. J. Refract. Met. Hard Mater.* **2014**, *45*, 86–94. [CrossRef]
10. Yoganandh, J.; Natarajan, S.; Kumaresh Babu, S.P. Erosive wear behavior of high-alloy cast iron and duplex stainless steel under mining conditions. *J. Mater. Eng. Perform.* **2015**, *24*, 3588–3598. [CrossRef]
11. Fortini, A.; Suman, A.; Vulpio, A.; Merlin, M.; Pinelli, M. Microstructural and erosive wear characteristics of a high chromium cast iron. *Coatings* **2021**, *11*, 490. [CrossRef]
12. Jia, R.N.; Liu, S.L.; Luo, Z.C.; Ning, J.P.; Wang, H.Y.; Luo, T.G.; Zhu, Y.S.; Yuan, X.S.; Wang, Z. Microstructure and wear resistance of WC and high chromium cast iron hardfacing layers. *Coatings* **2020**, *10*, 852. [CrossRef]
13. Pintaude, G.; Tschiptschin, A.P.; Tanaka, D.K.; Sinatora, A.S. The particle size effect on abrasive wear of high-chromium white cast iron mill balls. *Wear* **2001**, *250*, 66–70. [CrossRef]
14. Sapate, S.G.; RamaRao, A.V. Erosive wear behaviour of weld hardfacing high chromium cast irons: Effect of erodent particles. *Tribol. Int.* **2006**, *39*, 206–212. [CrossRef]
15. Zhi, X.H.; Liu, J.Z.; Xing, J.D.; Ma, S.Q. Effect of cerium modification on microstructure and properties of hypereutectic high chromium cast iron. *Mater. Sci. Eng. A* **2014**, *603*, 98–103. [CrossRef]
16. Zhi, X.H.; Xing, J.D.; Gao, Y.M.; Fu, H.G.; Peng, J.Y.; Xiao, B. Effect of heat treatment on microstructure and mechanical properties of a Ti-bearing hypereutectic high chromium white cast iron. *Mater. Sci. Eng. A* **2008**, *487*, 171–179. [CrossRef]
17. Wiengmoon, A.; Pearce, J.T.H.; Chairuangsri, T. Relationship between microstructure, hardness and corrosion resistance in 20 wt.%Cr, 27 wt.%Cr and 36 wt.%Cr high chromium cast irons. *Mater. Chem. Phys.* **2011**, *125*, 739–748. [CrossRef]
18. Zhang, A.F.; Xing, J.D.; Gao, Y.M.; Su, J.Y. Mechanism and electrochemical behavior of inter-phase corrosion of chromium white cast irons. *Acta Metall. Sin.* **2000**, *36*, 765–769.
19. Zhang, A.F.; Xing, J.D. A quantitative investigation on the dynamic inter-phase corrosion of chromium white cast irons. *Acta Metall. Sin.* **2001**, *37*, 77–81.
20. Liu, Z.L.; Li, Y.X.; Chen, X.; Hu, K.H. Microstructure and mechanical properties of high boron white cast iron. *Mater. Sci. Eng. A* **2008**, *486*, 112–116. [CrossRef]
21. Fu, H.G.; Li, Z.H.; Jiang, J.Q.; Xing, J.D. Solidification structure in a cast B-bearing stainless steel. *Mater. Lett.* **2007**, *61*, 4504–4507. [CrossRef]
22. Fu, H.G.; Li, Z.H.; Lei, Y.Q.; Jiang, Z.Q.; Xing, J.D. Structural variations in heat treated B-bearing stainless steel. *Mater. Des.* **2009**, *30*, 885–891.
23. Yi, Y.L.; Xing, J.D.; Wan, M.J.; Yu, L.L.; Lu, Y.F.; Jian, Y.X. Effect of Cu on microstructure, crystallography and mechanical properties in Fe-B-C-Cu alloys. *Mater. Sci. Eng. A* **2017**, *708*, 274–284. [CrossRef]
24. Ma, S.Q.; Xing, J.D.; He, Y.L.; Fu, H.G.; Li, Y.F.; Liu, G.Z. Effect of orientation and lamellar spacing of Fe_2B on interfaces and corrosion behavior of Fe-B alloy in hot-dip galvanization. *Acta Mater.* **2016**, *115*, 392–402. [CrossRef]
25. Lentz, J.; Röttger, A.; Großwendt, F.; Theisen, W. Enhancement of hardness, modulus and fracture toughness of the tetragonal $(Fe,Cr)_2B$ and orthorhombic $(Cr,Fe)_2B$ phases with addition of Cr. *Mater. Des.* **2018**, *156*, 113–124. [CrossRef]
26. Jian, Y.X.; Huang, Z.F.; Xing, J.D.; Zheng, B.C.; Sun, L.; Liu, Y.Z.; Liu, Y.M. Effect of improving Fe_2B toughness by chromium addition on the two-body abrasive wear behavior of Fe-3.0 wt%B cast alloy. *Tribol. Int.* **2016**, *101*, 331–339. [CrossRef]
27. Zhang, J.J.; Gao, Y.M.; Xing, J.D.; Wei, X.W.; Ma, S.Q.; Che, B.H. Effect of hot forging on microstructure and abrasion resistance of Fe-B alloy. *Tribol. Trans.* **2013**, *56*, 461–468. [CrossRef]

28. Lu, S.Y. *Super Stainless Steel and High Nickel Corrosion Resistant Alloy*, 1st ed.; Chemical Industry Press: Beijing, China, 2012; pp. 7–23.
29. Günen, A.; Kurt, B.; Orhan, N.; Kanca, E. The investigation of corrosion behavior of borided AISI 304 austenitic stainless steel with nanoboron powder. *Prot. Met. Phys. Chem. Surf.* **2014**, *50*, 104–110. [CrossRef]
30. Günen, A.; Karakaş, M.S.; Kurt, B.; Calik, A. Corrosion behavior of borided AISI 304 austenitic stainless steel. *Anti-Corros. Methods Mater.* **2014**, *61*, 112–118. [CrossRef]
31. American Society for Testing and Materials. *ASTM E384–08, Standard test Method for Microindentation Hardness of Materials*; American Society for Testing and Materials: West Conshohocken, PA, USA, 2008.
32. Li, Y.F.; Gao, Y.M. Three–body abrasive wear behavior of CC/high–Cr WCI composite and its interfacial characteristics. *Wear* **2010**, *268*, 511–518. [CrossRef]
33. Richardson, R.C.D. The wear of metals by hard abrasives. *Wear* **1967**, *10*, 291–309. [CrossRef]